ORGANIC CHEMISTRY FRONTIERS

RESEARCH ARTICLE

View Article Online
View Journal

Cite this: DOI: 10.1039/d5qo01437a

Controlling structural and photophysical properties in sequentially methylated phenoxazines

Alexander Huber,[a] Felix van der Vight,[a] Viktoria Heising,[a] Christoph Wölper,[b] Oleg Prymak,[b] Hatem M. A. Amin,[b] Kenneth E. Maly[c] and Jens Voskuhl*[a]

The "magic methyl" effect is widely regarded as one of the most extraordinary features in small-molecule drug design and has recently been recognized as a subtle yet powerful tool for fine-tuning the photophysical properties of luminophores. In this context, we investigated how steric pressure influences the structural and photophysical attributes in a series of sequentially methylated phenoxazines. Structural elucidation using X-ray diffraction revealed that the steric strain of *ortho*-positioned methyl groups induces out-of-plane twisting of the *N*-arylated rings, which significantly alters the packing interactions by preventing dense π stacking. Complementary quantum chemical calculations indicate changes in the antiaromatic character due to partial rehybridization of the bridging nitrogen atom from sp^2 to a more trigonal pyramidal geometry. Steady-state and time-resolved spectroscopy further highlighted the correlations between out-of-plane bending and emissive behavior, as characterized by distinctly pronounced changes in molar absorptivity and Stokes shifts. Finally, an effective strategy to overcome steric hindrance was demonstrated by extending the overall molecular conjugation, resulting in intense emission with high absolute photoluminescence quantum yields in both solution and the solid state.

Received 15th October 2025,
Accepted 7th December 2025

DOI: 10.1039/d5qo01437a

rsc.li/frontiers-organic

Introduction

In recent years, the utilization of the methyl group, one of the simplest functional organic units in chemistry, has attracted tremendous interest in small-molecule drug design.[1] Numerous reports mentioned that implementing a single methyl group into a drug candidate can lead to a significant increase in its pharmacological properties, often improving biological activity and potency through changes in solubility, selectivity, stability, conformation, and binding affinity.[2,3] Although intra- and intermolecular interactions of methyl groups were largely overlooked in the past due to the relatively weak nature of London dispersion forces, C–H···π interactions were proven to be of paramount importance in molecular recognition.[4] A prominent example is found in DNA, where the methyl substituent at the 5-position of the nucleotide base thymine aids in stabilizing the double helix.[5] In contrast, less stable RNA has incorporated uracil units that lack methyl groups at this specific position. The seemingly inexplicable improvements in particular attributes resulting from the incorporation of methyl substituents have led to the phenomenon being colloquially referred to as the "magic methyl effect".[6] Beyond biological applications, methyl groups are utilized to improve energy storage properties in materials science,[7] modulate the rotation of molecular motors in supramolecular chemistry,[8] and are frequently incorporated into luminescent scaffolds for the precise tailoring of their photophysical properties.[9,10]

Based on previous findings of steric demand caused by aromatic backbones in dihydrodibenzo[*a*,*c*]phenazines,[11,12] Tian's group reported on the conformational changes and varying photophysical properties of *ortho*-methylated 5,10-dihydrophenazines.[13] These compounds can undergo excited-state planarization from V-shaped geometries in their ground states, resulting in long-wavelength emission through vibration-induced emission (VIE).[14,15] Specifically, the steric strain of the *ortho*-positioned methyl groups induced bent geometries in the electronic ground-states S_0, causing hypsochromic shifts of the absorption maxima from 416 to 324 nm. Surprisingly, these distorted structures exhibited an even higher tendency for structural twisting in the excited state than the sterically unaffected parent compounds, leading to bathochromically

[a]*Faculty of Chemistry (Organic Chemistry), CENIDE and Center of Medical Biotechnology (ZMB), University of Duisburg-Essen, Universitätsstraße 7, 45141 Essen, Germany. E-mail: jens.voskuhl@uni-due.de*
[b]*Faculty of Chemistry (Inorganic Chemistry), University of Duisburg-Essen, Universitätsstraße 7, 45141 Essen, Germany*
[c]*Department of Chemistry and Biochemistry, Wilfrid Laurier University, 75 University Avenue W., Waterloo, ON N2L 3C5, Canada*

shifted emission maxima and thus large Stokes shifts. Hua and coworkers[16] leveraged these attributes for photodynamic therapy (PDT) under both normoxic and hypoxic conditions by employing compounds that exhibited aggregation-induced emission (AIE),[17,18] which were capable of mitochondrial targeting and generating type I reactive oxygen species (ROS).

Bryce's group observed similar effects of steric pressure in phenoxazinyl-substituted dibenzothiophene-*S*,*S*-dioxides, which can adopt pyramidal or axial conformations, resulting in blue-shifted absorbances and enlarged Stokes shifts.[19] Although the methylated congeners displayed less pronounced thermally activated delayed fluorescence (TADF), replacing oxygen-containing phenoxazine (POA) groups with sulfur-containing phenothiazine (PTA) groups enabled intense room temperature phosphorescence (RTP) in the presence of *ortho*-methyl groups.

These phenothiazine systems are known for their inherent ability to switch between quasi-equatorial and quasi-axial conformations based on the substitution pattern.[20,21] Recently, Li and colleagues examined the influence of steric hindrance on the parent phenothiazine core, which allowed for gradual changes in folding angles from 180° to 90°.[22] In particular, moving the *ortho*-methyl group from the PTA core to the *N*-arylated substituted ring inverted the preferred geometrical arrangement (from axial to equatorial and *vice versa*) upon photoexcitation.[23]

Maly's group reported several studies on *N*,*N*-diaryl diazadioxatetrahydropentacene luminophores derived from terephthalonitrile scaffolds, investigating the effect of methylated *N*-arylated substituents on the crystal structures and fundamental photophysical characteristics.[24,25] Building on this work, we recently examined the effects of meticulously balancing the steric hindrance caused by *ortho*-positioned methyl groups on the photophysical properties of similar alkylated heteropentacyclic luminophores.[26] Steric pressure not only enabled emission color tuning from red to green, but also served as a design principle for novel structures that demonstrate photoluminescence insensitive to the microenvironment. In general, this concept refers to the ability of a material to exhibit solution and solid-state emission (SSSE).[27–29] This indicates that photoluminescence is the favored deexcitation pathway, whether in diluted monomeric conditions or in the solid state, including polycrystalline powders, single crystals, aggregates, thin films, or when embedded in materials.[30,31] In the past, it was often reported that novel luminophores were effective emitters in either solution or the solid state, but not both. This limitation arises from issues such as aggregation-caused quenching (ACQ)[32,33] or AIE, also known as solid-state luminescence enhancement (SLE).[34] Consequently, achieving omnipotent emission is a highly desirable key attribute for organic luminescent materials, as it enables overcoming the challenges of quenching in applications such as organic light-emitting diodes (OLEDs),[35] bioimaging,[36,37] or photocatalysis.[38,39]

This study emphasizes steric strain as a fundamental design principle, motivating our investigation into how sequentially relocated methyl groups affect the structural and photophysical properties of functionalized phenoxazines. Molecular geometries and structural changes were examined using single-crystal X-ray diffraction (scXRD) and density functional theory (DFT), and correlated with the photophysical properties using steady-state and time-resolved spectroscopic techniques.

Results and discussion

Synthesis and design

The structural and photophysical response to steric pressure was evaluated by comparing the properties of two primary *N*-phenyl substituted phenoxazine compounds **POA-*XX***, differing in the absence (**POA-00**) or presence (**POA-10**) of an *ortho*-positioned methyl group next to the central oxazine core (Scheme 1). Additionally, the response of relocating the methyl group to alternative positions was assessed. In reference compound **POA-1′0**, the methyl group was set in the *para* position of the oxazine nitrogen atom, allowing for controlling purely electron donating effects. Further relocation was performed in the *ortho* position of the peripheral *N*-aryl ring (**-*X*1**), resulting in the tolyl-substituted derivative **POA-01** and xylyl-functionalized **POA-02**. Penultimately, an attempt was made to surmount the steric hindrance of the *ortho*-positioned methyl group by combining the phenoxazine scaffold **POA-1*X*** with the *N*-tolyl (**POA-11**) or *N*-xylyl (**POA-12**) substituent. The series was completed by forcing a conjugation of both the terminal aminophenol-backbone and the *N*-aryl substituent through a covalent bond. This was realized by the design of the indolophenoxazine compound **In-POA**.

The synthesis was carried out starting from either 2-aminophenol (**1a**), 3-methyl-2-aminophenol (**1b**), or 5-methyl-2-aminophenol (**1c**) for all **POA-*XX*** compounds (Scheme 1). The specific *N*-arylations were achieved in high yields (>65%) by using the respective iodobenzenes (**2a–2c**) as reagents and employing copper-catalyzed Ullmann–Goldberg conditions, following modified procedures from Li *et al.*[40] These *N*-arylated aminophenol derivatives were subsequently converted into the target phenoxazines *via* nucleophilic aromatic substitution reactions with 2,3,5,6-tetrafluoroterephthalonitrile (TFTN). Under these reaction conditions, competitive formation of the corresponding heteropentacyclic side products was observed,[26] resulting in a low yield (17%) for **POA-02** and moderate yields (40–70%) for the other compounds. Although the purifications of all products were feasible using column chromatography, **POA-10** co-eluted with its corresponding heteropentacene by-product as an inseparable mixture, necessitating recrystallization for complete purification.

The synthesis of the indolo-compound **In-POA** commenced with tosylation of *o*-bromoaniline (**4**), which gave *N*-tosylated aniline **5** in 96% yield. Compound **5** was reacted with 3-hydroxyphenylboronic acid to furnish biphenyl **6** in 46% yield, following procedures from Youn *et al.*[41] Then, palladium-catalyzed C–H amidation was utilized for the formation of protected hydroxy–carbazole **7** (73%). Finally, deprotection of the

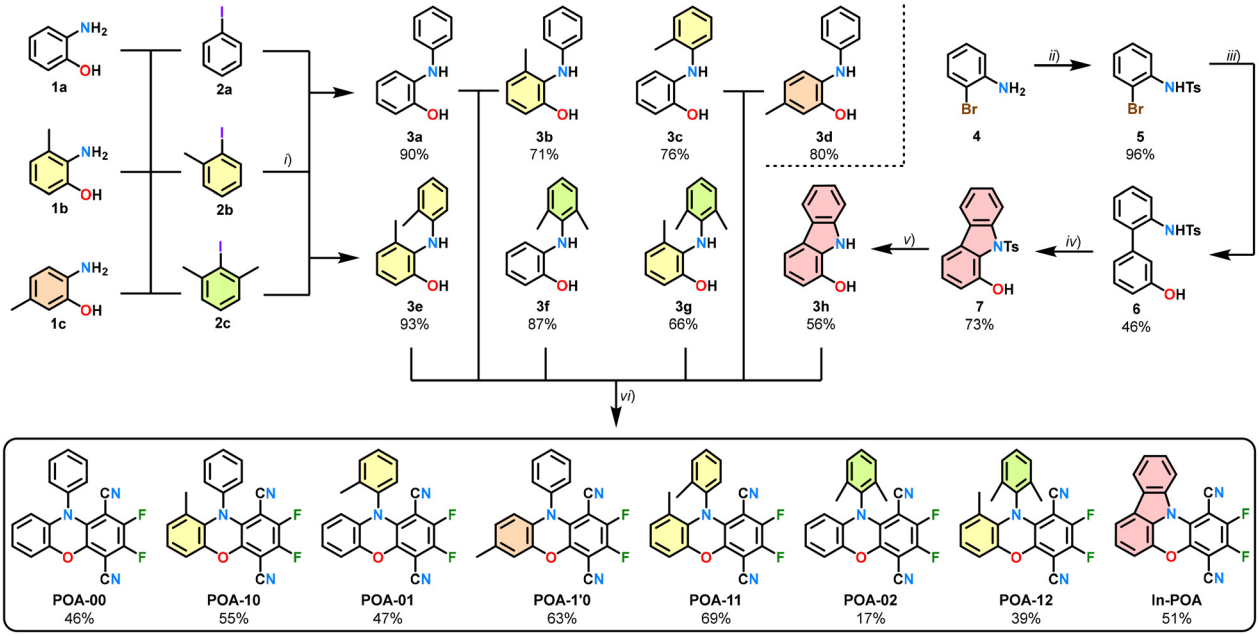

Scheme 1 Synthesis route and isolated yields for all compounds in this study: (i) 2 eq. of **1a–1c**, 1 eq. of **2a–2c**, CuI (0.2 eq.), K_3PO_4 (2 eq.), DMF, 80 °C, 18 h; (ii) *p*-TsCl (1.3 eq.), pyridine (0.2 m), 25 °C, 18 h; (iii) 3-hydroxyphenylboronic acid (1.5 eq.), Na_2CO_3 (2.1 eq.), $Pd(OAc)_2$ (0.05 eq.), acetone/H_2O 1/1, 35 °C, 18 h; (iv) bathocuproine (0.1 eq.), Na_2CO_3 (1 eq.), $Pd(OAc)_2$ (0.1 eq.), mesitylene, 100 °C, 36 h; (v) Mg (30 eq.), THF/MeOH (1/1), 70 °C, 18 h; (vi) 1–2 eq. of **3a–3h**, 2,3,5,6-tetrafluoroterephthalonitrile (1 eq.), K_2CO_3 (3–6 eq.), DMF, 25–100 °C, 18–72 h.

N-tosyl group (56% yield) allowed the reaction of hydroxy-carbazole **3h** with TFTN, giving **In-POA** in 51% yield (see the SI for detailed procedures). All final products were characterized using IR spectroscopy, high-resolution mass spectrometry, ^{1}H, ^{13}C, and ^{19}F NMR spectroscopy (Fig. S2–S13), and the signals were assigned using 2D NMR techniques. High-performance liquid chromatography (Fig. S14) ensured high sample purity (>99%).

X-ray diffractometric analysis

Single crystals of seven compounds were grown and measured using X-ray diffractometry. Deposition numbers CCDC 2490301–2490307 contain the crystallographic data used for this study. Except for **POA-02**, which was crystallized by slow evaporation from a concentrated acetone solution, the crystals were grown by slow diffusion of overlayered solvent mixtures. For **POA-10**, a chloroform solution was overlayered with cyclohexane, whereas for the other compounds, dichloromethane was used as the base solvent and overlayered with cyclohexane (**POA-00**), butanone (**POA-01**), methanol (**POA-1′0**, **In-POA**), or ethyl acetate/chlorobenzene (**POA-12**). Despite several attempts, no suitable crystals of **POA-11** were obtained due to poor sample scattering. However, by serendipitous discovery, the heteropentacyclic side product was crystallized and measured using X-ray diffractometry (deposition number CCDC 2490263, see Fig. S40).[42] Fig. 1 displays the molecular crystal structures of selected compounds with perpendicular and in-plane views of the luminophore unit (see Fig. S39 for the remaining compounds).

Compounds **POA-00** and **-10** crystallize in the monoclinic space group $P2_1/c$, albeit **POA-10** crystallized with two molecules in the asymmetric unit, showing pseudo-translational symmetry along *b* (see Table S14 for more information). The methyl group at position C11 in **POA-10** induces a discernible bending of the heteroaromatic core by pushing the *N*-aryl substituent out of plane. This is apparent from the measured angles α_{ONC} of the bridging oxygen (O1) and nitrogen atoms with the *ipso*-carbon atom of the aromatic substituent (C15), which reduces from almost in-plane (177°) in **POA-00** to out-of-plane (120°) in **POA-10** (Table 1). Additionally, the steric pressure induces a bending of the oxazine ring, resulting in a generally less planar structure. This is indicated by the increase in the fold angle θ_{AP-TN} (5° compared with 22°) as a planarity indicator, which was determined by defining mean planes for both the aminophenol and terephthalonitrile rings. Consequently, the adjacent nitrile group is less bent in **POA-10** (α_{CCN} = 176°) than in **POA-00** (172°), because repulsive interactions are reduced.

Interestingly, the steric hindrance is countered in **POA-12** by the bulky xylyl-substituent, which aids in maintaining a somewhat in-plane geometry (α_{ONC} = 176°), although it causes a distorted structure (θ_{AP-TN} = 11°). This is particularly surprising since the related xylyl-substituted compound **POA-02** without the core-methyl group at position C11 displays a comparably higher out-of-plane twisting (α_{ONC} = 155°), similarly to Maly's reported heteropentacyclic congener.[24] Both xylyl-substituted compounds, as well as **POA-01** and **POA-1′0**, crystallized in the triclinic space group $P\bar{1}$. In the latter two, relocat-

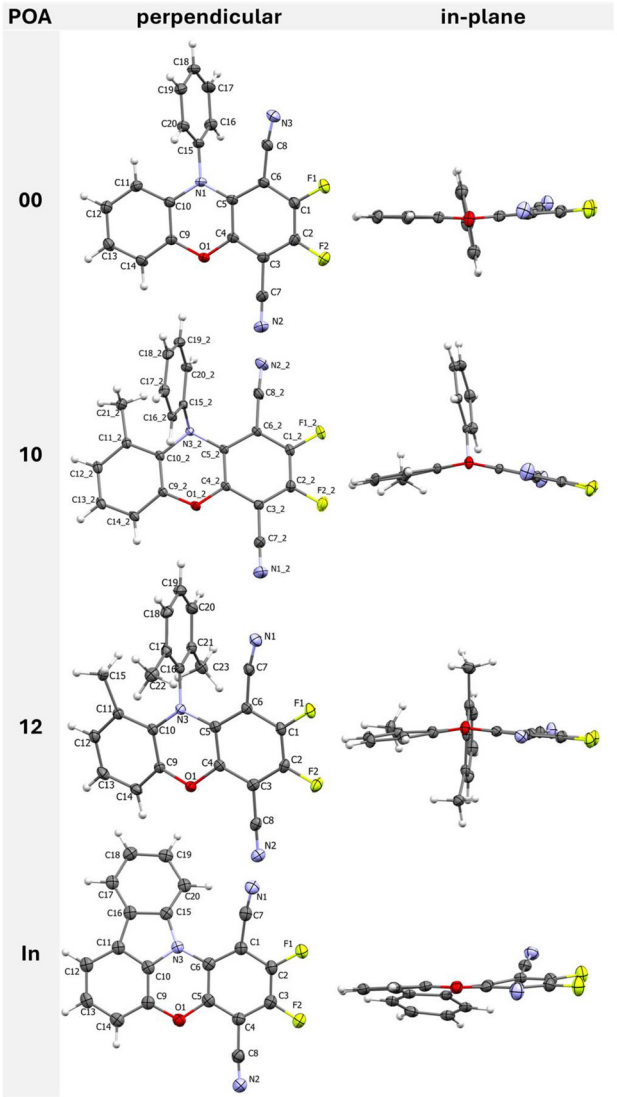

Fig. 1 Molecular crystal structures of the compounds **POA-00**, **-10**, **-12**, and **In-POA** (perpendicular and in-plane views). The displacement ellipsoids are displayed at 50% probability levels.

Table 1 Top: measured angles [°] in the X-ray diffractometric structures: α_{ONC} = plane angle of the O1/bridging nitrogen/*ipso* carbon atom; α_{CCN} = bending angle of the adjacent nitrile-group; θ_{AP-TN} = fold angle between the calculated mean planes of terminal aminophenol and terephthalonitrile rings. Bottom: illustration of the respective angles for **POA-10**

Compound	α_{ONC}	α_{CCN}	θ_{AP-TN}
POA-00	177	172	5.1
POA-10	120	176	22
POA-01	175	170	6.4
POA-1′0	176	172	0.4
POA-02	155	172	9.3
POA-12	176	172	11
In-POA	160	173	8.1

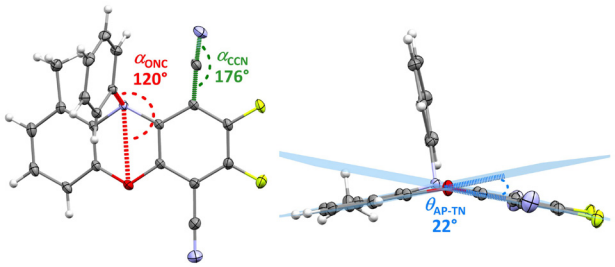

ing the methyl group away from position C11 eliminates the steric demand, resulting in similar structural parameters to those of **POA-00**. Implementing a covalent bond between the aminophenol ring and the *N*-aryl substituent forms the indolo-compound **In-POA**, which crystallized in the orthorhombic space group *Pbca* (see Table S15 for more information). Since the thin plate diffracted poorly, quantitative results should be interpreted with caution. Overall, all rings are forced into conjugation, but the repulsive interactions with the adjacent nitrile group induce a slight helical distortion in the molecular backbone.

Additionally, the intermolecular contacts in crystal structures were analyzed to identify the most relevant interactions in the crystal packing, particularly the changes that occur when methyl groups are introduced. Generally, the compounds with planar geometries (**POA-00**, **-01**, **-1′0**) form columns dominated by inverted *anti-co*-facial oriented π···π interactions (see Fig. S41A and S43A–S44A, blue lines). The alternating orientation of the terminal rings enhances the electrostatic interactions between the electron-deficient terephthalonitrile ring and the electron-rich aminophenol ring. The π stacks are interconnected by either fluorine- or nitrile-driven contacts (see Fig. S41B and S43B–S44B, orange lines), forming sheets that extend into three-dimensional networks through hydrogen bonding (green and red lines). These interaction motifs are consistent with reported packing analyses of related phenoxazine-based derivatives.[43] The introduction of a methyl group into tolyl-substituted phenoxazine **POA-01** leads to a slightly larger π···π distance (3.71 Å) compared to that of **POA-00** (3.57 Å, see Tables S16, S17, S20 and S21). To compensate for this increase, the methyl group is involved in additional nitrile-driven hydrogen bonds (2.87 Å, 2.88 Å, see Fig. S43 and Table S21). Compound **POA-1′0** with the highest overall planarity also exhibits the closest π···π contacts (3.56 Å, Fig. 2A and Tables S22, S23).

Significant packing divergences emerge with increasing molecular distortion, as observed in the xylyl-functionalized molecules **POA-02** and **-12** (see Fig. S45 and S46). The lower in-plane angle α_{ONC} in **POA-02** (155°) causes one methyl group to shield the core system from classic π···π stacking. Instead, CN···π stacking (3.49 Å, 3.55 Å, Tables S24 and S25) primarily characterizes dimer-like arrays interlocked by hydrogen bonds (purple line, see Fig. S45A). Similar CN···π stacking occurs in **POA-12**, but due to the higher core planarity, the contacts are closer (3.39 Å, 3.39 Å, see Fig. S46A, Tables S26 and S27). The dimers are interconnected by C–H···π (3.00 Å) and slipped π···π contacts (3.43 Å, 1.75 Å offset), forming a tilted staircase

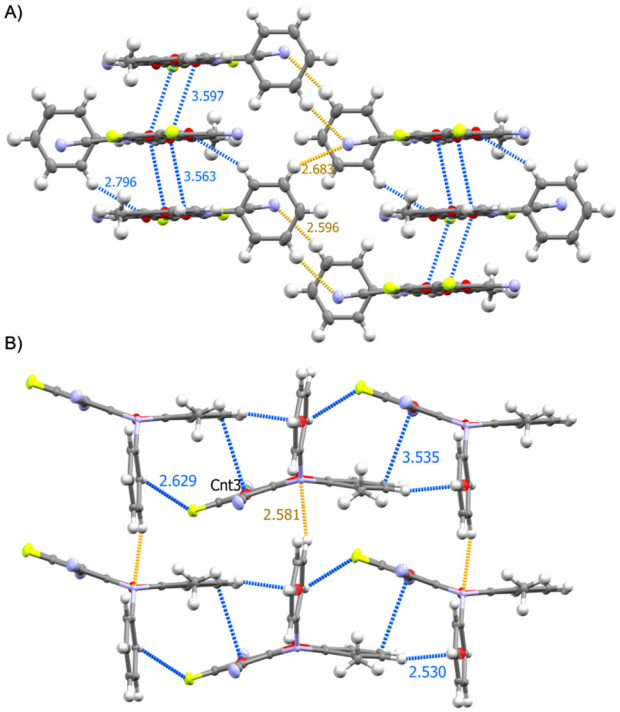

Fig. 2 Excerpt of the crystal packings of (A) **POA-1′0** and (B) **POA-10**, showcasing the formation of (A) π stacked arrays with oxygen-driven hydrogen bonds between dimeric structures (blue lines) interconnected by nitrile-mediated hydrogen bonds (orange lines); (B) brick-like formation of trimeric layers with offset π···π contacts (blue), interconnected by nitrogen-driven hydrogen bonds (orange lines). The displacement ellipsoids are displayed at 50% probability levels.

(purple lines). Although the methyl groups are involved in hydrogen bonding, the large spacing results in a significantly fewer intermolecular interactions. As a result, F···F interactions (2.85 Å) are present in the formation of sheets.

The highly conjugated structure **In-POA** shows the expected high degree of again inverted *anti-co*-facial oriented π···π stacking (3.44 Å, 3.59 Å, Tables S28 and S29), forming distorted honeycomb-like sheets through hydrogen bonding (see Fig. S47, blue lines).

The most discernible deviations in the crystal packing are again evident in **POA-10**. Due to the distorted central geometry, π stacked arrays are not formed. Instead, a brick-like pattern is present (see Fig. S42), comprising trimeric units with considerable slipped π···π (3.54 Å, 14° angle of mean planes) and C–H···π interactions (2.53 Å, blue lines, Fig. 2B and Tables S18, S19). The individual layers are interlinked by close hydrogen bonding originating from the bridging nitrogen atom of the oxazine core (2.58 Å, orange lines, Fig. 2B). This nitrogen atom exhibits a trigonal pyramidal geometry with partial sp^3 hybridization (*vide infra*), which improves its ability to accept hydrogen bonds compared to the nitrogen atom in **POA-00**. Moreover, the layers expand to a three-dimensional network through nitrile-mediated interactions, including hydrogen bonding and π contacts (see purple lines, Fig. S42B). Notably, the individual interactions of the two independent molecules in the asymmetric unit differ only slightly and can be considered approximately equivalent. Energy decomposition analysis (EDA)[44] calculations for trimers of compounds **POA-00** (Fig. 2A) and **POA-10** (Fig. 2B) confirmed that the total interaction energy of **POA-10** is decreased due to reduced π stacking (see Table S35). The interaction energies are dominated by dispersion.

Powder X-ray diffractometry was used to quantify the crystallinity of the bulk powders (see Fig. S48). All data indicate similar crystalline phases, as observed in the single crystals. Although the PXRD pattern could not be simulated for **POA-11**, the experimental peak profile is similar to that of **POA-01**. For **POA-01**, **-1′0**, **-12**, and **In-POA**, additional minor phases were observed (marked with asterisks). All extracted crystallite sizes indicate the presence of microcrystalline domains (>100 nm).

Quantum chemical calculations

Density functional theory (DFT)[45] calculations within the *Gaussian 16*[46] program were performed to elucidate structural and electronic effects induced by steric strain. All calculations employed the functional PBE0[47] with the TZVP[48] basis set, which has proven reliable for calculating related phenoxazines.[30] Dispersion correction (D3BJ)[49] was considered for ground-state calculations, whereas excited states were evaluated using time-dependent density functional theory (TD-DFT).[50] All optimized geometries were confirmed as energetic minima by the absence of imaginary frequencies. Crystal structure geometries were applied as initial guesses, and the obtained geometries after optimizing the structural parameters generally match those acquired from X-ray diffractometry (*vide supra*). In the case of **POA-11**, a bent starting geometry analogous to **POA-10** was adopted, based on the structure of the aforementioned heteropentacyclic side product (Fig. S40).[42] The optimized bending angle for **POA-11** was 129°, indicating a preferred out-of-plane twisting, albeit less pronounced than for **POA-10** (117°).

To quantify the steric effects of the *ortho*-methylated structures **POA-10**, **-11**, and **-12**, relaxed potential energy scans were performed for the out-of-plane bending of the *N*-arylated rings. The plane angle α_{ONC} of 178° in **POA-00** was sequentially reduced in 5° increments over 20 steps. Methyl groups were attached to their respective positions, and the geometry was optimized at each step. The resulting energies are plotted in Fig. 3 as a function of the bending angle α_{ONC}, relative to the energy at the initial geometry.

In the absence of an *ortho*-methyl group, such as for **POA-00**, the out-of-plane bending leads to the expected energetic destabilization. In contrast, the out-of-plane bending in **POA-10** stabilizes the structure significantly by 5.1 kcal mol^{-1} at an energetic minimum near α_{ONC} = 118°, similar to that for previously reported substituted heteropentacenes.[26] Interestingly, **POA-11** displays energetic minima at both respective angles of interest (129° and 178°). Due to steric pressure, the out-of-plane conformation is again preferred, with a stabilization energy of 2.5 kcal mol^{-1} at 129° compared

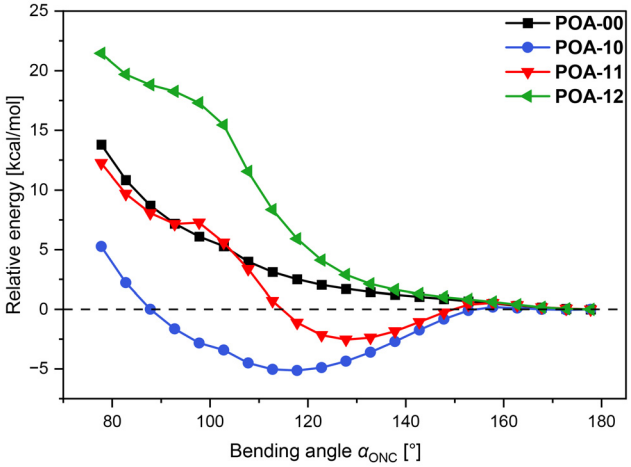

Fig. 3 Relative energies of the optimized geometries at every relaxed scan step of the bending angle α_{ONC} for compounds **POA-00** (black), **-10** (red), **-11** (blue), and **-12** (green), calculated using PBE0-D3BJ/TZVP.

with the conformer optimized at 178°. The parameters of both conformers were then optimized without restraints to estimate their relative populations at room temperature. The resulting Gibbs free energy difference of 1.0 kcal mol^{-1} corresponds to Boltzmann populations of 84% (α_{ONC} = 129°) and 16% (α_{ONC} = 178°), respectively, indicating the coexistence of both conformers. In the case of two methyl groups present at the *N*-aryl ring, as in **POA-12**, out-of-plane bending becomes disfavoured due to repulsive interactions, as demonstrated by the evident destabilization (Fig. 3, green curve). Hence, the *N*-xylyl substitution facilitates surmounting structural rearrangements induced by steric strain.

Since steric pressure affects the molecular geometry, a natural bond order (NBOs) analysis was conducted (Fig. 4). In **POA-00**, the lone pair of the bridging oxazine nitrogen atom exhibits almost pure p-character (>99%), consistent with sp^2-hybridization of this atom. In contrast, while this lone pair still shows predominant p-character (90%) in **POA-10**, an additional s-character (10%) also contributes. Consequently, the nitrogen atom showcases partial sp^2/sp^3-like hybridization,

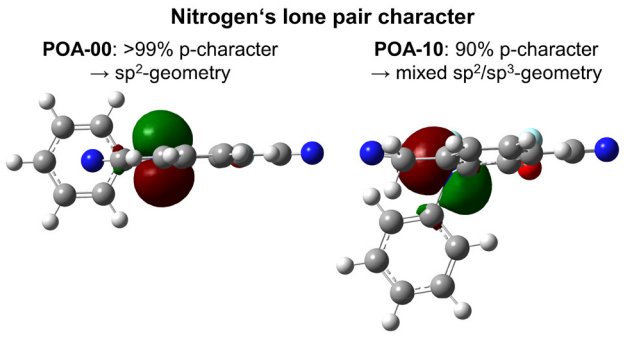

Fig. 4 Comparison of the lone pair character of the bridging oxazine nitrogen atom for **POA-00** (left) and **POA-10** (right) from the in-plane view, calculated using PBE0-D3BJ/TZVP.

which significantly perturbs the electronic properties of this molecule.

Fig. 5 illustrates the stabilizing out-of-plane bending in **POA-10** by the significant decrease in energy of the highest occupied molecular orbital (HOMO, −6.7 eV), which is reduced by 0.6 eV compared with that of **POA-00** (−6.1 eV, Table S32). In cyclic voltammetry experiments (the potential reported here is normalized *vs.* Fc/Fc$^+$), **POA-00** indeed exhibits a lower reversible redox potential (+0.803 V) than **POA-10** (+0.934 V, Fig. S51), consistent with the qualitative theoretical HOMO ordering, see details in SI. In contrast, the energies of the lowest unoccupied molecular orbitals (LUMOs) are less influenced by the steric demand. This is because the LUMOs are localized at the terephthalonitrile side, which experiences less impact from the geometrical rearrangement due to steric effects, as displayed by the virtual natural transition orbitals (NTOs, see Fig. S49 and S50). In total, the HOMO–LUMO energy gap increases for **POA-10**, coinciding with a hypsochromic shift of the absorption maximum (from λ_{ab} = 421 nm for **POA-00** to λ_{ab} = 399 nm for **POA-10**).

The sterically induced geometrical reorganization also affects the aromaticity of the oxazine core, as assessed by computing nucleus-independent chemical shifts (NICS) 1 Å above the ring centroids.[51,52] The calculated NICS(1) value of −10.0 ppm of the model compound benzene using GIAO-PBE0/TZVP matched the literature value, signifying aromaticity.[53] For **POA-00**, the central oxazine ring shows a NICS (1) value of 6.2 ppm, denoting an antiaromatic character as expected for phenoxazines. In contrast, a NICS(1) index of −0.2 ppm was obtained for **POA-10**, indicating a non-aromatic character. Analogous trends were obtained from using the out-

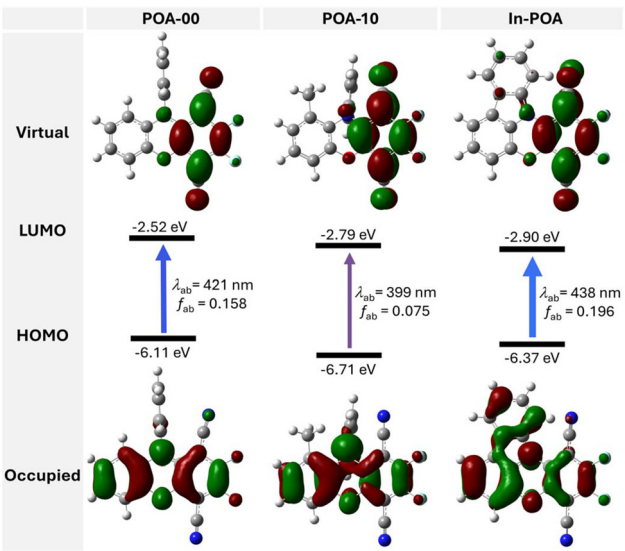

Fig. 5 Calculated optimized geometries in the S_0 states with the corresponding virtual and occupied natural transition orbital (NTO) pairs, energies of the HOMOs and LUMOs, as well as calculated absorption wavelengths λ_{ab} and oscillator strengths f_{ab} (calculated using TD-PBE0/TZVP) for compounds **POA-00**, **POA-10**, and **In-POA**.

of-plane component of the shielding tensors as indicated by the corresponding NICS(1)$_{zz}$ values (see Table S31).[54] Although NICS indices quantitatively indicate (anti)aromaticity, their single scalar descriptors of magnetic responses must be interpreted cautiously in heteroaromatic systems with partial pyramidalization.[55] Accordingly, the trends were corroborated by complementary bond length analysis using the harmonic oscillator model of aromaticity (HOMA, see eqn (S1), Table S30 for details).[52,56]

POA-10 showcases a disrupted conjugation compared with **POA-00**, which also results in a reduced oscillator strength f_{ab} (0.075 *versus* 0.158) for the monoelectronic excitation involving the HOMOs to the LUMOs (see Table S32). Notably, compound **In-POA** displays the most extended conjugation through the contribution of the terminal carbazole ring to the HOMO (Fig. 5), leading to the highest overall increased oscillator strength for absorption (f_{ab} = 0.196). In terms of theoretical absorption wavelengths, all calculated $\lambda_{ab,calc}$ values show good agreement with the experimentally determined absorption maxima in THF (see Table S33). Additionally, the geometrical parameters of the compounds were optimized in their respective excited singlet states S_1. All **POA-*XX*** derivatives display rotations of the *N*-arylated rings in the S_1 states, which correlate with large Stokes shifts. Indeed, the theoretical emission wavelengths $\lambda_{em,calc}$ generally match the emission wavelengths measured for the THF solutions, except for **POA-10** ($\Delta\lambda_{em,THF-calc}$ = 0.421 eV). This deviation is attributed to the well-known underestimation of charge transfer excitation energies in the selected computational method, as a quinoid structure is formed (see Fig. S49). The deviation can be overcome by using the CC2/def2-TZVP method, which provides more accurate results (see Table S34).[57,58]

Investigation of the photophysical properties

Ultimately, the effect of steric pressure on the photophysical properties of the compounds was investigated, commencing with optically diluted solutions. To cover a range of different solvent polarities, cyclohexane (CH), tetrachloromethane (CCl_4), dichloromethane (DCM), tetrahydrofuran (THF), acetonitrile (MeCN) and methanol (MeOH) were selected. UV/Vis absorption spectra were recorded in all solvents, exhibiting similar features with intense, strong, and sharp absorption bands around 235 nm along with broader, less intense absorption maxima at 390–450 nm (Fig. S15). Generally, the measured absorption maxima follow the trends predicted by the DFT calculations (*vide supra*). The λ_{ab} values for the in-plane compounds, such as **POA-00**, are around 450 nm in DCM and shift towards 396 nm for **POA-10** (Fig. 6A). Compound **POA-11** displays an expected in-between behavior (λ_{ab} = 427 nm, see Table S1).

Additionally, molar absorption coefficients ε were determined for all compounds in THF solutions (Fig. S16 and S17). The out-of-plane bending leads to a considerable reduction in ε when comparing **POA-00** with **-10** (5940 *versus* 3380 L mol^{-1} cm^{-1}). Noteworthy, **In-POA** demonstrates the highest overall ε with a value of 10 040 L mol^{-1} cm^{-1}. Hence, the molar absorption coefficients agree well with the calculated oscillator strengths.

Steady-state and time-resolved photoluminescence spectroscopy studies were employed to examine the excited-state properties. All lifetimes τ_{av_amp} are in the nanosecond range up to 10 ns, confirming fluorescence as the dominant radiative deactivation mechanism (Fig. S30–S37). All compounds demonstrate analogous solvatochromism, showing turquoise emission in cyclohexane, green in CCl_4, yellow luminescence in DCM, and dark yellow in MeOH (see Fig. S18–S25). This color change in emission with increasing solvent polarity reflects the progressive stabilization of intramolecular charge-transfer (ICT) states.[59] The structured emission bands observed in non-polar solvents correspond to vibronic progressions. In contrast, in polar solvents such as acetonitrile and methanol, the emission bands become broader and less

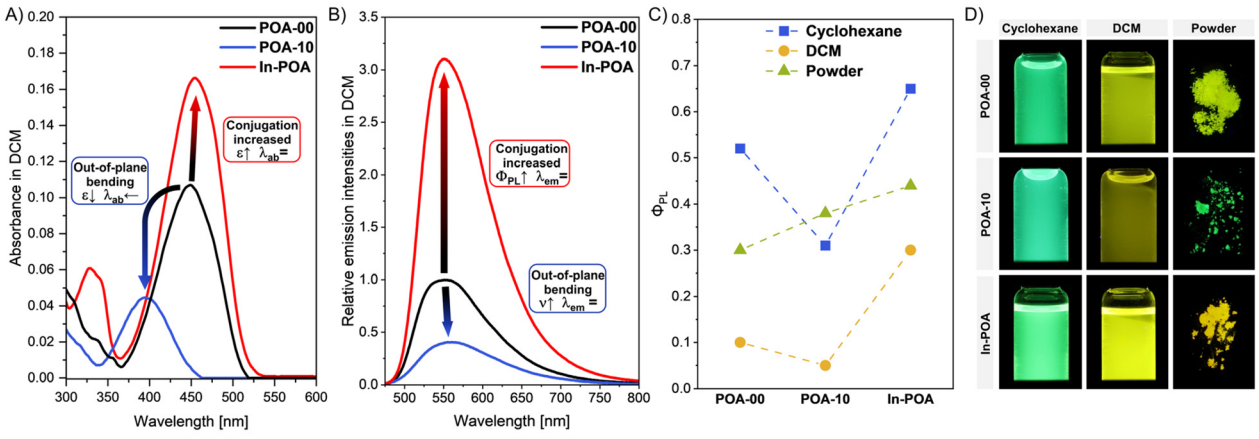

Fig. 6 Selected display of the photophysical properties of compounds **POA-00**, **POA-10**, and **In-POA**: (A) UV/Vis spectra in DCM (15 μM); (B) photoluminescence spectra in DCM (15 μM) relative to **POA-00**; (C) absolute photoluminescence quantum yields Φ_{PL} in cyclohexane, DCM, and as powders; (D) photographs of the three compounds in cyclohexane (left column), in DCM (centred column), and as powders (right column) under UV-light (365 nm).

structured, accompanied by reduced intensities, indicating that enhanced non-radiative relaxation processes occur in these environments. Most interestingly, **POA-00** and **-10** exhibit approximately identical emission wavelengths in all solvents (Table S2), although displaying distinct absorption differences (Fig. 6B). Consequently, **POA-10** possesses Stokes shifts that are nearly twice as high as those of **POA-00** (Table 2). The Stokes shifts were plotted as a function of the orientation polarization factors Δf using the Lippert–Mataga equation (Fig. S26 and Table S11).[60] The slope and intercept values of **POA-00** are around 4000 cm^{-1}, increasing to approximately 6000 cm^{-1} for **POA-10**. On the one hand, the steeper slope of **POA-10** indicates a more pronounced polarity enhancement upon excitation compared with **POA-00**, suggesting increased sensitivity to solvent polarity. On the other hand, the larger intercept of **POA-10** reflects an intrinsically higher ground-state polarity, aligning with a larger inherent dipole moment change associated with the twisted geometry.[61]

The enhanced geometrical rearrangements of **POA-10** result in generally lower absolute photoluminescence quantum yields Φ_{PL} (see Fig. S38 for an exemplary report file) and reduced radiative deactivation rate constants k_r compared with **POA-00** (Table 2). In contrast, relatively high Φ_{PL} values up to 0.65 (**In-POA**) were measured for the non-polar cyclohexane and CCl_4 solutions, highlighting the strongly emissive nature of the compounds (see Tables S3–S10). Particularly, **In-POA** showcases the best overall Φ_{PL} and k_r values, even reaching a Φ_{PL} value of 0.12 in acetonitrile (Table S10), which matches the calculated high oscillator strength f_{em} (0.146). Because **In-POA** possesses a covalent bond between the phenoxazine stator unit and the rotor *N*-aryl ring, non-radiative dissipation through rotation is suppressed in solution, which is evident by the generally lower k_{nr} values (Table 2). Table 2 summarizes selected photophysical parameters of the compounds **POA-00**, **POA-10**, and **In-POA**.

Additionally, the photophysical properties of the powders were assessed (Table S12). It is worth noting that all compounds displayed strong solvent dependency in terms of their optical properties, resulting in various poly-microcrystalline habits. To ensure comparability, the compounds were measured after rapid evaporation of their DCM solutions. In general, all compounds show intense emission in the solid state (Fig. S27). As already observed in the crystal packings, the out-of-plane twisted ring of **POA-10** averts dense π stacking, resulting in a higher Φ_{PL} value for the powder of **POA-10** (0.38) compared with **-00** (0.30). Since geometric relaxations in the solid state are more restricted than in solution, the emission color of **POA-10** appears green (λ_{em} = 516 nm) instead of yellow, as seen for **POA-00** (λ_{em} = 548 nm). Compounds **POA-11** and **-01** both show photophysical properties similar to those of **-00** as powders, although possessing higher k_{nr} values, which may be due to the presence of additional methyl groups in the rotor unit. Orange emission colors are displayed by **POA-1′0**, **-02**, and **-12**, whereas **In-POA** again exhibits the highest Φ_{PL} (0.44) and k_r values (0.64×10^8 s^{-1}). Due to the pronounced absolute photoluminescence quantum yield values in most solvents and the solid state, **In-POA** demonstrates the best SSSE properties among the presented compounds (Fig. 6D).

This trend is further supported by comparing the emissive behavior in aggregation studies (at 15 μM) using binary THF/water mixtures (Fig. S28). While increasing water content (20–60%) initially causes polarity-induced quenching, aggregation at higher water contents restores or even enhances emission in most cases.[62] However, because all measurements were conducted using a fixed excitation wavelength, the Φ_{PL} values must be discussed for accurate comparison (Table S13). Here, all aggregates formed at THF/H_2O 10/90 show significantly higher Φ_{PL} values than the THF solutions, except for **In-POA** (0.22, 0.32, respectively; see Fig. S29 for the corresponding sizes at the 10/90 THF/H_2O ratios using dynamic light scattering, DLS).

Table 2 Overview of selected photophysical properties of compounds **POA-00**, **POA-10**, and **In-POA** in cyclohexane, DCM (each 15 μM) and as powders: wavelengths λ [nm] for absorption λ_{ab}, excitation λ_{ex}, and emission λ_{em}, Stokes shifts $\Delta\nu$ [cm^{-1}], absolute photoluminescence quantum yields Φ_{PL}, and amplitude-weighted average fluorescence lifetimes τ_{av_amp} [ns]

		POA-00	POA-10	In-POA
Cyclohexane	λ_{ab} [nm]	436	388	441
	λ_{em} [nm]	516	499	518
	$\Delta\nu_{ab-em}$ [cm^{-1}]	3556	5733	3371
	Φ_{PL}	0.52 ± 0.03	0.31 ± 0.02	0.65 ± 0.03
	$k_r(k_{nr})$[10^8 s^{-1}]	0.59 (0.54)	0.35 (0.78)	0.69 (0.37)
	τ_{av_amp} [ns]	8.88 ± 0.01	8.88 ± 0.01	9.40 ± 0.01
DCM	λ_{ab} [nm]	449	396	454
	λ_{em} [nm]	553	559	551
	$\Delta\nu_{ab-em}$ [cm^{-1}]	4189	7363	3878
	Φ_{PL}	0.10 ± 0.02	0.05 ± 0.02	0.30 ± 0.02
	$k_r(k_{nr})$[10^8 s^{-1}]	0.4 (3.6)	0.2 (4.3)	0.53 (1.24)
	τ_{av_amp} [ns]	2.50 ± 0.01	2.22 ± 0.02	5.64 ± 0.01
Powder	λ_{ex} [nm]	512	462	533
	λ_{em} [nm]	548	516	565
	$\Delta\nu_{ex-em}$ [cm^{-1}]	1283	2265	1063
	Φ_{PL}	0.30 ± 0.02	0.38 ± 0.02	0.44 ± 0.02
	k_r (k_{nr}) [10^8 s^{-1}]	0.24 (0.56)	0.41 (0.67)	0.64 (0.81)
	τ_{av_amp} [ns]	12.59 ± 0.05	9.21 ± 0.04	6.89 ± 0.02

Conclusions

In conclusion, this study elucidated how sterically demanding *ortho*-positioned methyl groups influence the structural and photophysical properties of eight phenoxazine-derived luminophores. Single-crystal X-ray diffractometry revealed that the *ortho*-methyl groups induce significant geometrical distortions through out-of-plane twisting and disrupt π···π dominated interactions in the crystal packing. Complementary DFT calculations disclosed partial rehybridization of the oxazine nitro-

gen atom, transitioning from planar sp^2 to a trigonal pyramidal sp^2/sp^3 geometry, accompanied by a loss of the antiaromatic character. While all compounds exhibit pronounced photoluminescence in various molecular environments, the geometric and electronic perturbations manifested in distinct photophysical responses. **POA-10** exemplifies the most substantial impact of steric pressure through enlarged Stokes shifts. In contrast, the rigid derivative **In-POA** highlights the strongest and most balanced solution and solid-state emission behavior due to increased conjugation. Hence, this study comprises a modular approach to leverage the efficient steric strain of methyl groups as a strategy for fine-tuning structural and photophysical properties. Establishing steric pressure as a molecular design principle is anticipated to further advance the development of stimuli-responsive and microenvironment-insensitive materials in smart photonic systems and optoelectronic applications.

Author contributions

A. Huber: conceptualization, data curation, formal analysis, investigation, methodology, visualization, writing – original draft, and writing – review and editing; F. v. d. Vight: conceptualization, formal analysis, and investigation; V. Heising: investigation and formal analysis; C. Wölper: data curation and validation; O. Prymak: data curation and formal analysis; H. M. A. Amin: data curation, electrochemical measurements, and visualization; K. E. Maly: validation and writing – review & editing; J. Voskuhl: conceptualization, resources, supervision, and writing – review & editing.

Conflicts of interest

There are no conflicts to declare.

Data availability

The data supporting this article have been included as part of the supplementary information (SI). Supplementary information: detailed synthetic procedures and additional analytical data regarding spectroscopic characterization, X-ray diffractometric analyses, quantum chemical calculations, and cyclic voltammetry. See DOI: **https://doi.org/10.1039/d5qo01437a**.

CCDC 2490301–2490307 contain the supplementary crystallographic data for this paper.[63a–g]

Acknowledgements

We thank Finn Rethemeier for his assistance during synthesis and Lea Höfmann and Sophia Stadtfeld for their help with the analyses. Prof. Dr Gebhard Haberhauer is acknowledged for his support and fruitful discussions regarding quantum chemical calculations. Additionally, we thank Dr Constantin G. Daniliuc for determining the crystal structure of the heteropentacyclic side product of compound **POA-11**. Prof. Dr Georg Jansen is acknowledged for his financial support.

References

1 E. J. Barreiro, A. E. Kümmerle and C. A. M. Fraga, The Methylation Effect in Medicinal Chemistry, *Chem. Rev.*, 2011, **111**, 5215–5246.
2 P. de S. M. Pinheiro, L. S. Franco and C. A. M. Fraga, The Magic Methyl and Its Tricks in Drug Discovery and Development, *Pharmaceuticals*, 2023, **16**, 1157.
3 C. S. Leung, S. S. F. Leung, J. Tirado-Rives and W. L. Jorgensen, Methyl Effects on Protein–Ligand Binding, *J. Med. Chem.*, 2012, **55**, 4489–4500.
4 M. Nishio, Y. Umezawa, M. Hirota and Y. Takeuchi, The CH/π interaction: Significance in molecular recognition, *Tetrahedron*, 1995, **51**, 8665–8701.
5 Y. Umezawa and M. Nishio, Thymine-methyl/π interaction implicated in the sequence-dependent deformability of DNA, *Nucleic Acids Res.*, 2002, **30**, 2183–2192.
6 H. Schönherr and T. Cernak, Profound Methyl Effects in Drug Discovery and a Call for New C-H Methylation Reactions, *Angew. Chem., Int. Ed.*, 2013, **52**, 12256–12267.
7 J. J. Lee, K. Jeong, S. Kwon, H. Yook, S. M. Kim, J. W. Han, J. Choi and J. H. Park, 'Magic methyl effect' in 2-benzylpyridine-based H_2 storage materials: Enhanced H_2 storage/release performances, *Energy Storage Mater.*, 2024, **67**, 103259.
8 Y. Gisbert, M. Fellert, C. N. Stindt, A. Gerstner and B. L. Feringa, Molecular Motors' Magic Methyl and Its Pivotal Influence on Rotation, *J. Am. Chem. Soc.*, 2024, **146**, 12609–12619.
9 Y. Li, R. W. Weerasinghe, Y. Hu, X. Tan, B. Cai, C. Adachi and C.-Y. Chan, The magic methyl effect of thermally activated delayed fluorescent emitters on blue organic light-emitting diodes, *J. Mater. Chem. C*, 2025, **13**, 12691–12698.
10 S. Bhuin, S. Bhattacharya and M. Chakravarty, Acceptor–donor–acceptor-linked triphenylamine and phenothiazine motifs as cousin molecules: the methyl effect on stimuli-responsiveness, crystallochromism, and dual-state emission, *New J. Chem.*, 2021, **45**, 21236–21247.
11 Z. Chen, X. Jin, R. Shen, W. Li, L. Sun, J. Su, D.-H. Qu, Z. Zhang and H. Tian, Capturing the Progressive Conformational Evolutions of Sterically-Congested Dihydrophenazines via Crystallization, *Angew. Chem., Int. Ed.*, 2025, **64**, e202424597.
12 Z. Zhang, Y.-S. Wu, K.-C. Tang, C.-L. Chen, J.-W. Ho, J. Su, H. Tian and P.-T. Chou, Excited-State Conformational/Electronic Responses of Saddle-Shaped *N*,*N*′-Disubstituted-Dihydrodibenzo[*a*,*c*]phenazines: Wide-Tuning Emission from Red to Deep Blue and White Light Combination, *J. Am. Chem. Soc.*, 2015, **137**, 8509–8520.
13 X. Jin, S. Li, L. Guo, J. Hua, D.-H. Qu, J. Su, Z. Zhang and H. Tian, Interplay of Steric Effects and Aromaticity

Reversals to Expand the Structural/Electronic Responses of Dihydrophenazines, *J. Am. Chem. Soc.*, 2022, **144**, 4883–4896.

14 Z. Zhang, W. Song, J. Su and H. Tian, Vibration–Induced Emission (VIE) of *N*,*N*′–Disubstituted–Dihydribenzo[*a*,*c*] phenazines: Fundamental Understanding and Emerging Applications, *Adv. Funct. Mater.*, 2020, **30**, 1902803.

15 X. Jin, S. Guo, X. Wang, M. Cong, J. Chen, Z. Zhang, J. Su, D. Qu and H. Tian, Sequential Multistep Excited–State Structural Transformations in *N*,*N*′–Diphenyl–dihydrodibenzo[*a*,*c*]phenazine Fluorophores, *Angew. Chem., Int. Ed.*, 2023, **62**, e202305572.

16 S. Li, X. Jin, Z. Zhang, J. Li and J. Hua, An AIE-active type I photosensitizer based on N,N′-diphenyl-dihydrophenazine for high-performance photodynamic therapy under hypoxia, *Mater. Chem. Front.*, 2023, **7**, 3738–3746.

17 J. Luo, Z. Xie, J. W. Y. Lam, L. Cheng, H. Chen, C. Qiu, H. S. Kwok, X. Zhan, Y. Liu, D. Zhu and B. Z. Tang, Aggregation-induced emission of 1-methyl-1,2,3,4,5-pentaphenylsilole, *Chem. Commun.*, 2001, 1740–1741.

18 J. Mei, N. L. C. Leung, R. T. K. Kwok, J. W. Y. Lam and B. Z. Tang, Aggregation-Induced Emission: Together We Shine, United We Soar!, *Chem. Rev.*, 2015, **115**, 11718–11940.

19 J. S. Ward, R. S. Nobuyasu, M. A. Fox, A. S. Batsanov, J. Santos, F. B. Dias and M. R. Bryce, Bond Rotations and Heteroatom Effects in Donor–Acceptor–Donor Molecules: Implications for Thermally Activated Delayed Fluorescence and Room Temperature Phosphorescence, *J. Org. Chem.*, 2018, **83**, 14431–14442.

20 Y. Wang, J. Yang, M. Fang, Y. Gong, J. Ren, L. Tu, B. Z. Tang and Z. Li, New Phenothiazine Derivatives That Exhibit Photoinduced Room–Temperature Phosphorescence, *Adv. Funct. Mater.*, 2021, **31**, 2101719.

21 L. Mayer, L. May and T. J. J. Müller, The interplay of conformations and electronic properties in *N*-aryl phenothiazines, *Org. Chem. Front.*, 2020, **7**, 1206–1217.

22 Y. Gao, W. Yuan, Y. Li, A. Huang, Y. Fang, A. Li, K. Wang, B. Zou, Q. Li and Z. Li, Accurately adjusted phenothiazine conformations: reversible conformation transformation at room temperature and self-recoverable stimuli-responsive phosphorescence, *Light: Sci. Appl.*, 2025, **14**, 99.

23 M. Gao, R. Wu, Y. Zhang, Y. Meng, M. Fang, J. Yang and Z. Li, New Molecular Photoswitch Based on the Conformational Transition of Phenothiazine Derivatives and Corresponding Triplet Emission Properties, *J. Am. Chem. Soc.*, 2025, **147**, 2653–2663.

24 L. K. Hiscock, V. S. Patel, A. M. Raj, C. Amoah, A. J. Talreja, W. G. Skene and K. E. Maly, Luminescent *N*-aryl-heteroacene derivatives, *Can. J. Chem.*, 2023, **101**, 186–197.

25 L. K. Hiscock, C. Yao, W. G. Skene, L. N. Dawe and K. E. Maly, Synthesis of Emissive Heteroacene Derivatives via Nucleophilic Aromatic Substitution, *J. Org. Chem.*, 2019, **84**, 15530–15537.

26 A. Huber, T. Thiele, T. Rex, C. G. Daniliuc, C. Wölper, R. Y. Lorberg, L. Höfmann, C. A. Strassert, M. Giese and J. Voskuhl, Steric Pressure in Heteropentacenes Modulates the Photophysical Properties – A Molecular Design Strategy for Functional Materials, *Chem. Sci.*, 2025, **16**, 15723–15733.

27 A. Huber, J. Dubbert, T. D. Scherz and J. Voskuhl, Design Concepts for Solution and Solid–State Emitters – A Modern Viewpoint on Classical and Non–Classical Approaches, *Chem. – Eur. J.*, 2023, **29**, e202202481.

28 J. L. Belmonte-Vázquez, Y. A. Amador-Sánchez, L. A. Rodríguez-Cortés and B. Rodríguez-Molina, Dual-State Emission (DSE) in Organic Fluorophores: Design and Applications, *Chem. Mater.*, 2021, **33**, 7160–7184.

29 T. Stoerkler, T. Pariat, A. D. Laurent, D. Jacquemin, G. Ulrich and J. Massue, Excited-State Intramolecular Proton Transfer Dyes with Dual-State Emission Properties: Concept, Examples and Applications, *Molecules*, 2022, **27**, 2443.

30 A. Huber, L. Schmidt, T. Gatz, J. Bublitz, T. Rex, S. T. N. Sailaja, E. Verheggen, L. Höfmann, C. Wölper, C. A. Strassert, S. K. Knauer and J. Voskuhl, Stepwise Modulation of Bridged Single–Benzene–Based Fluorophores for Materials Science, *Chem. – Eur. J.*, 2025, **31**, e202404263.

31 S. T. N. Sailaja, I. Maisuls, J. Kösters, A. Hepp, A. Faust, J. Voskuhl and C. A. Strassert, Naphthalonitriles featuring efficient emission in solution and in the solid state, *Beilstein J. Org. Chem.*, 2020, **16**, 2960–2970.

32 J. B. Birks, *Photophysics of aromatic molecules*, Wiley-Interscience, London, New York, 1970.

33 J. Gierschner, L. Lüer, B. Milián-Medina, D. Oelkrug and H.-J. Egelhaaf, Highly Emissive H-Aggregates or Aggregation-Induced Emission Quenching? The Photophysics of All-Trans para-Distyrylbenzene, *J. Phys. Chem. Lett.*, 2013, **4**, 2686–2697.

34 J. Gierschner, J. Shi, B. Milián-Medina, D. Roca-Sanjuán, S. Varghese and S. Park, Luminescence in Crystalline Organic Materials: From Molecules to Molecular Solids, *Adv. Opt. Mater.*, 2021, **9**, 2002251.

35 I. S. Park, S. Y. Lee, C. Adachi and T. Yasuda, Full–Color Delayed Fluorescence Materials Based on Wedge–Shaped Phthalonitriles and Dicyanopyrazines: Systematic Design, Tunable Photophysical Properties, and OLED Performance, *Adv. Funct. Mater.*, 2016, **26**, 1813–1821.

36 A. Huber, J. Koch, K. Rudolph, A. Höing, F. Rizzo, S. K. Knauer and J. Voskuhl, Deoxyestrone-based lipofection agents with solution- and solid-state emission properties, *Org. Biomol. Chem.*, 2023, **21**, 5762–5767.

37 J. Dubbert, A. Höing, N. Graupner, Ľ. Rajter, M. Dunthorn, S. K. Knauer, A. Galstyan, F. Rizzo and J. Voskuhl, Cationic Solution and Solid-State Emitters – Robust Imaging Agents for Cells, Bacteria, and Protists, *Chem. – Eur. J.*, 2023, **29**, e202300334.

38 M. N. Khatun, S. Nandy, C. Srinivas, S. Kumar and P. K. Iyer, Molecularly Engineered Photosensitizers Based on Superoxide Generation, Solid State White Light Emission, Excimer-Driven Photosensitization, and Photoredox Catalysis, *Adv. Opt. Mater.*, 2025, **13**, e01052.

39 J.-M. Heo, J. Park, M. F. Flórez-Angarita, L. Wang, C. Yu, J. Choi, H. Woo, B. Milián-Medina, A. J. Matzger, M. S. Kwon, J. Gierschner and J. Kim, Elucidating the molecular structural origin of efficient emission across solid and solution phases of single benzene fluorophores, *Nat. Commun.*, 2025, **16**, 5560.

40 Y. Li, H. Wang, L. Jiang, F. Sun, X. Fu and C. Duan, Copper–Catalyzed Direct Synthesis of Di– and Triphenylamines: A Dramatic Accelerating Effect of 2–Aminophenols, *Eur. J. Org. Chem.*, 2010, 6967–6973.

41 S. W. Youn, Y. H. Kim and Y. H. Jo, Palladium-Catalyzed Regioselective Synthesis of 1-Hydroxycarbazoles Under Aerobic Conditions, *Adv. Synth. Catal.*, 2019, **361**, 462–468.

42 A. Huber, C. G. Daniliuc and J. Voskuhl, CCDC 2490263: Experimental Crystal Structure Determination, *CSD Commun.*, DOI: **10.5517/ccdc.csd.cc2plb2q**.

43 L. K. Hiscock, K. E. Maly and L. N. Dawe, Crystal Packing of a Series of 1,2,3,4-Substituted Phenoxazine and Dibenzodioxin Heterocycles, *Cryst. Growth Des.*, 2019, **19**, 7298–7307.

44 F. M. Bickelhaupt and E. J. Baerends, in *Reviews in Computational Chemistry*, John Wiley & Sons, Ltd, 2000, pp. 1–86.

45 M. Bursch, J. Mewes, A. Hansen and S. Grimme, Best–Practice DFT Protocols for Basic Molecular Computational Chemistry, *Angew. Chem., Int. Ed.*, 2022, **61**, e202205735.

46 M. J. Frisch, G. W. Trucks, H. B. Schlegel, G. E. Scuseria, M. A. Robb, J. R. Cheeseman, G. Scalmani, V. Barone, G. A. Petersson, H. Nakatsuji, X. Li, M. Caricato, A. V. Marenich, J. Bloino, B. G. Janesko, R. Gomperts, B. Mennucci, H. P. Hratchian, J. V. Ortiz, A. F. Izmaylov, J. L. Sonnenberg, D. Williams-Young, F. Ding, F. Lipparini, F. Egidi, J. Goings, B. Peng, A. Petrone, T. Henderson, D. Ranasinghe, V. G. Zakrzewski, J. Gao, N. Rega, G. Zheng, W. Liang, M. Hada, M. Ehara, K. Toyota, R. Fukuda, J. Hasegawa, M. Ishida, T. Nakajima, Y. Honda, O. Kitao, H. Nakai, T. Vreven, K. Throssell, J. A. Montgomery Jr., J. E. Peralta, F. Ogliaro, M. J. Bearpark, J. J. Heyd, E. N. Brothers, K. N. Kudin, V. N. Staroverov, T. A. Keith, R. Kobayashi, J. Normand, K. Raghavachari, A. P. Rendell, J. C. Burant, S. S. Iyengar, J. Tomasi, M. Cossi, J. M. Millam, M. Klene, C. Adamo, R. Cammi, J. W. Ochterski, R. L. Martin, K. Morokuma, O. Farkas, J. B. Foresman and D. J. Fox, *Gaussian 16, Revision A.03*, Gaussian, Inc., Wallingford CT, 2016.

47 J. P. Perdew, K. Burke and M. Ernzerhof, Generalized Gradient Approximation Made Simple, *Phys. Rev. Lett.*, 1996, **77**, 3865–3868.

48 A. Schäfer, C. Huber and R. Ahlrichs, Fully optimized contracted Gaussian basis sets of triple zeta valence quality for atoms Li to Kr, *J. Chem. Phys.*, 1994, **100**, 5829–5835.

49 S. Grimme, S. Ehrlich and L. Goerigk, Effect of the damping function in dispersion corrected density functional theory, *J. Comput. Chem.*, 2011, **32**, 1456–1465.

50 F. Furche and R. Ahlrichs, Adiabatic time-dependent density functional methods for excited state properties, *J. Chem. Phys.*, 2002, **117**, 7433–7447.

51 Z. Chen, C. S. Wannere, C. Corminboeuf, R. Puchta and P. von R. Schleyer, Nucleus-Independent Chemical Shifts (NICS) as an Aromaticity Criterion, *Chem. Rev.*, 2005, **105**, 3842–3888.

52 R. Gleiter and G. Haberhauer, *Aromaticity and other conjugation effects*, Wiley, Weinheim, 2012.

53 R. Gleiter, G. Haberhauer and S. Woitschetzki, From Eight-Membered 10π Electron Sulfur–Nitrogen Cycles to Bicycles and Cages: A Theoretical Approach, *Chem. – Eur. J.*, 2014, **20**, 13801–13810.

54 R. Gershoni-Poranne and A. Stanger, Magnetic criteria of aromaticity, *Chem. Soc. Rev.*, 2015, **44**, 6597–6615.

55 A. Stanger, NICS – Past and Present, *Eur. J. Org. Chem.*, 2020, 3120–3127.

56 T. M. Krygowski and M. K. Cyrański, Structural Aspects of Aromaticity, *Chem. Rev.*, 2001, **101**, 1385–1420.

57 F. Weigend and R. Ahlrichs, Balanced basis sets of split valence, triple zeta valence and quadruple zeta valence quality for H to Rn: Design and assessment of accuracy, *Phys. Chem. Chem. Phys.*, 2005, **7**, 3297–3305.

58 O. Christiansen, H. Koch and P. Jørgensen, The second-order approximate coupled cluster singles and doubles model CC2, *Chem. Phys. Lett.*, 1995, **243**, 409–418.

59 S. K. Behera, S. Y. Park and J. Gierschner, Dual Emission: Classes, Mechanisms, and Conditions, *Angew. Chem., Int. Ed.*, 2021, **60**, 22624–22638.

60 Z. N. Scheller, D. Liese, H. Siera, N. Semleit, M. Schmiedtchen, C. Wölper and G. Haberhauer, The Origin of Dual-Emission in PLICT Compounds – an Empirical Approach, *Chem. – Eur. J.*, 2024, **30**, e202304143.

61 J. R. Lakowicz, *Principles of fluorescence spectroscopy*, Springer, New York, 3rd edn, 2006.

62 J. Maillard, K. Klehs, C. Rumble, E. Vauthey, M. Heilemann and A. Fürstenberg, Universal quenching of common fluorescent probes by water and alcohols, *Chem. Sci.*, 2021, **12**, 1352–1362.

63 (*a*) CCDC 2490301: Experimental Crystal Structure Determination, 2025, DOI: **10.5517/ccdc.csd.cc2plc9z**; (*b*) CCDC 2490302: Experimental Crystal Structure Determination, 2025, DOI: **10.5517/ccdc.csd.cc2plcb0**; (*c*) CCDC 2490303: Experimental Crystal Structure Determination, 2025, DOI: **10.5517/ccdc.csd.cc2plcc1**; (*d*) CCDC 2490304: Experimental Crystal Structure Determination, 2025, DOI: **10.5517/ccdc.csd.cc2plcd2**; (*e*) CCDC 2490305: Experimental Crystal Structure Determination, 2025, DOI: **10.5517/ccdc.csd.cc2plcf3**; (*f*) CCDC 2490306: Experimental Crystal Structure Determination, 2025, DOI: **10.5517/ccdc.csd.cc2plcg4**; (*g*) CCDC 2490307: Experimental Crystal Structure Determination, 2025, DOI: **10.5517/ccdc.csd.cc2plch5**.